26-047

Physical Modeling of Complex Coal Rib Brow Failure and Its Applicability to Numerical Modeling

Cameron Mitchel
Department of Mining and Explosives Engineering, Missouri University of Science and Technology

Alper Kirmaci
Department of Mining and Explosives Engineering, Missouri University of Science and Technology

Dogukan Guner
Department of Mining and Explosives Engineering, Missouri University of Science and Technology

Taghi Sherizadeh
Department of Mining and Explosives Engineering, Missouri University of Science and Technology

ABSTRACT

Brow hazards are a significant concern in coal mine ribs and form when weak coal sloughs out of a rib face and exposes an overhanging block of more competent rock or coal. Of 36 rib failure fatalities in the last two decades, 36% resulted from rib brow failures. This highlights the need to better understand the mechanisms driving brow formations and failures to mitigate this hazard and eliminate potential fatalities. The research team at Missouri S&T worked to enhance the current CPRR system and include the potential for these brow hazards. We employed physical modeling methods to build a scaled model from critical brow cases observed in the field. The dimensions and properties of the models were scaled down by 14.4 times from the field cases. The results of the physical modeling efforts were used to assist in calibrating distinct element numerical models vital to understanding brow formation and failure mechanisms. Subsequently, three physical models were created and tested to provide data on an otherwise impossible-to-capture event at the field scale. The results of these tests provided formed brow dimensions that agree well with those observed at the field scale. The brow dimensions were 1.25 inches deep into the rib, equivalent to 1.5 feet when scaled up. Similarly, the numerical modeling efforts provided good agreement by capturing a brow forming 1.55 inches deep into the rib. The physical model results further validate the applicability of physical modeling efforts for capturing otherwise difficult and dangerous phenomena in a controlled lab setting.

INTRODUCTION

In underground coal mines, rib instabilities are a serious safety concern. From incident reports between 2009 and 2020 collected directly from the MSHA fatality report database, rib-related incidents were responsible for an average fatality above one fatal injury per year and over 50 non-fatal injuries per year. In the 36 fatal rib failure accidents that occurred in U.S. coal mines between 1996 and 2022, 13 (36%) of the fatal injuries were a result of rib brow failures (Jones et al., 2014; MSHA, 2025). These statistics highlight the need to more clearly understand complex brow hazards and develop mitigation strategies to reduce the number of injuries and fatalities resulting from them.

Considering the dynamic nature of brow failures in coal mining conditions, it is extremely difficult to collect meaningful data in the field to capture the stages leading to brow formation and subsequent failure. To circumvent this limitation, physical modeling provides an effective means of simulating real coal mining conditions within a controlled laboratory environment where data can be collected and related to the field scale through empirical relationships. Many researchers working on coal strata control widely recognize the advantages of physical modeling (Fang et al., 2020; Huang et al., 2020; Kang et al., 2018; Kong et al., 2020; Li et al., 2022; Singh, T. & Farmer, I., 1985; Yang et al., 2018; Zhai et al., 2017). Based on the literature, these studies typically include key steps in the performance of physical test experiments, including similarity simulation, selection of model materials, deployment of monitoring systems, and execution of testing procedures.

The use of physical modeling provides an effective means of collecting critical data that is useful for understanding complex mechanisms such as brow failures. The successful collection of data also significantly aids numerical modeling efforts by providing another avenue for model calibration and verification. Toward this aim, a case study of an active coal mine was physically modeled, and the results were used to evaluate a coupled continuum and discontinuum numerical modeling approach for capturing and understanding brow failures.

PHYSICAL MODELING OF BROW CASE STUDY

Case Selection and Actual Material Properties

Three physical models were constructed and tested to simulate specific formed brow conditions observed in a coal seam in Southern West Virginia. The rib height of this selected critical case is 1.8 m (6 ft), and it is buried at a depth of 335 m (1100 ft) below the ground surface. A 2-D CAD drawing of the rib condition is presented in Figure 1.

Seven different units were simulated in the set of physical models. Most of the mechanical properties of these units were determined in our rock mechanics laboratory. Field observations and laboratory test results showed that the top and bottom shale units in the rib have identical material properties. As rock lump samples from the roof and floor shale units were unable to be collected, the mechanical properties of these units were taken from the literature. The material properties of each unit are presented in Table 1. According to Esterhuizen et al. (2013), models of coal measure rocks are not sensitive to the selection of Poisson's ratio. Notably, based on this, a default value of 0.25 is assumed for Poisson's ratio value for each unit.

Geomechanical Analogous Material

Physical models must meet a number of similarity requirements for geometry and physical and mechanical properties derived using force-equilibrium equations, geometry, and Hooke's law in accordance with the theory and dimensional analysis. The properties given in Table 1 were used to develop the equivalent model material properties. Considering the actual field conditions and capacity of the test system, the geometric scaling factor (C_l) and volume-weight scaling factor (C_γ) in this model experiment were set as 14.4 and 1.0, respectively. According to the similarity theory (Obert & Duvall, 1967), the similarity factors of other parameters were deduced as follows:

$$C_\sigma = C_E = C_l \times C_\gamma = 14.4 \ \times 1.0 \ = 14.4 \qquad (1)$$

$$C_\nu = C_\varepsilon = 1 \qquad (2)$$

where C_σ, C_E, C_ν, C_ε are the scaling constants of stress, elastic modulus, Poisson's ratio, and strain, respectively. Since proper scaling of cohesion and friction angle of the material is challenging for generating analogous models, the focus was on UCS and tensile strength, elastic modulus, and Poisson's ratio of materials when establishing similar

Table 1. Field scale material properties

Rock Unit	Thickness (m)	UCS (MPa)	Tensile Strength (MPa)	Young's Modulus (GPa)
Shale (Roof)	10	60	6.0	17.00
Shale (Rib)	0.6 & 0.3	21.17	2.17	2.55
Coal 1	0.4	5.35	0.54	1.15
Coal 2	0.5	7.82	0.78	1.50
Shale (Floor)	10	80	8.0	30.00

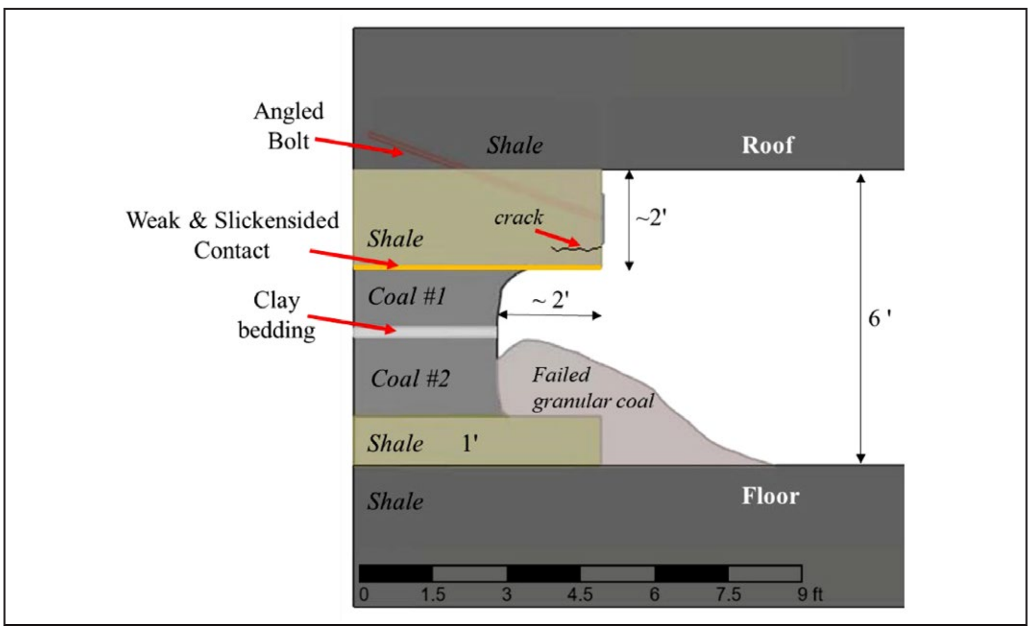

Figure 1. CAD drawing of the rib condition for the physical models

models. The calculated similar material parameters for the physical model are listed in Table 2. The model dimensions measured 76.2 cm tall, 152.4 cm wide, and 20.3 cm deep. Similarly, the rib height and excavation widths of the physical models were 10 cm and 30 cm, respectively, to ensure that the distance from the excavation boundary to the model boundary was around 3 times the excavation dimensions. This was necessary to minimize potential boundary effects in the physical model tests while balancing the scale of the physical model dimensions.

Laboratory Efforts for Achieving Analogous Material Properties

Several analogous materials were generated in laboratory trials to achieve materials with the desired mechanical properties of the rock types observed during surveys, as detailed in Table 2. Fine-grained sand (< 1 mm), plaster of Paris, ground coal and shale (< 1 mm), and water were mixed by specific ratios to simulate in-situ rocks with varying strengths. Prior research has noted that it can be difficult to ensure that all the mechanical properties of analogous materials meet the same criteria. As a result, in this study, the focus was on the uniaxial compressive strength (UCS) and Young's modulus of similar materials as significant indicators for creating comparable models. Cube molds are often used to assess the strength properties of different mixes in cement, mortar, grout, and concrete compound testing. In this study, we prepared 5 cm (2 in) cube samples by molding technique for strength testing consistent with this approach. Eight sets of analogous materials were created and subjected to uniaxial compressive strength testing. Six identical samples were prepared for each mixture, and three of them were tested. Accurately replicating the strength of these units was critical to ensure the physical models reflected the formed brow conditions from the selected case study.

Achieving Analogous Material Properties

The optimal materials ratio was determined through a trial-and-error process to achieve the desired mechanical parameters with a variance of less than 10% between the ideal and achieved mechanical parameters. The resulting material mixture ratios are presented in Table 3. The physical models consist of seven different units, and the achieved analogous material properties and corresponding mine scale properties of each unit are summarized in Table 4. In laboratory trials, over 20 analogous materials were produced with the aim of achieving materials with desired mechanical properties.

Table 2. The ideal mechanical parameters and thicknesses of similar materials

Rock Unit	Thickness (cm)	UCS (MPa)	Tensile Strength (MPa)	Young's Modulus (MPa)
Shale (Roof)	55	2.86	0.28	810
Shale (rib)	3.3 & 1.65	1.00	0.07	121
Coal 1	2.25	0.25	0.02	55
Coal 2	3.00	0.37	0.04	71
Shale (Floor)	55	3.81	0.20	1430

Table 3. Analogous material mixture ratios

	Analogous Materials Ratios (By Weight)				
Unit	Water	Sand	Coal	Shale	Plaster
Roof Shale	1.00	3.00	—	—	1.00
Rib Shale 1	1.00	4.00	—	0.50	0.50
Coal 1	1.00	4.00	0.75	—	0.35
Clay	1.00	4.00	0.4	—	0.60
Coal 2	1.00	4.00	0.75	—	0.35
Rib Shale 2	1.00	4.00	—	0.50	0.50
Floor Shale	1.00	3.00	—	—	1.00

Table 4. Summary of analogous and mine scale material properties for the physical models

	Analogous Material			Mine Scale		
Unit	Model Thickness (cm)	UCS (MPa)	Young's Modulus (GPa)	Unit Thickness (m)	UCS (MPa)	Young's Modulus (GPa)
Roof Shale	31.75	2.72	0.25	4.57	39.17	3.57
Rib Shale 1	4.23	1.00	0.05	0.61	14.40	0.76
Coal 1	2.54	0.37	0.03	0.37	5.33	0.44
Clay	0.42	0.12	0.01	0.06	1.73	0.17
Coal 2	3.39	0.37	0.03	0.49	5.33	0.44
Rib Shale 2	2.12	1.00	0.05	0.30	14.40	0.76
Floor Shale	31.75	2.72	0.25	4.57	39.17	3.57

Physical Model Experimental Scheme

Following the outlined procedure, the physical model seen below in Figure 2 was produced. Petroleum jelly was applied to the model frame to ensure no unwanted attachment of material, material components were weighed and dry-mixed to ensure no clumping occurred, water was added and a motorized mixer was used to ensure homogeneity of the resulting material mix. Material was poured layer-by-layer and smoothed with a spatula to ensure even surfaces, a steel frame was placed to maintain the excavation boundary, and the model was allowed to cure until moisture content was measured as 0% by a moisture meter. The physical model shown in Figure 2 is representative of the three models tested during this study.

TerraTek's high-capacity, displacement-controlled uniaxial testing frame was modified and adapted for the first two experiments. Conversely, a large-scale MTS load frame was used in the third experiment to better control the test's loading protocol. The physical system comprises a control unit, experimental platform, and data acquisition equipment (National Instruments or MTS Controller). Axial, lateral, and out-of-plane displacements were monitored using LVDTs, and a high-resolution video camera was used for 2-dimensional full-field displacement monitoring. Figure 3 illustrates the instrumentation and equipment setup used for the three physical model experiments.

In the first test, the roof was supported by two I-beams, while in the second and third experiments, the roof remained unsupported to eliminate compressive failure in the simulated roof unit due to the support members. Removing the I-beam supports did not adversely affect the model response. Conversely, it enabled the measurement of roof convergence and rib displacement in the second and third experiments, as no support member was present inside the excavation. This was accomplished by employing Fiber-Bragg-Grating-based displacement sensors, which enabled monitoring of the movement of the roof and ribs during the tests with micrometer sensitivity (Figure 3-b). The LVDT data collected from the experiments was used to verify the accuracy of Digital Image Correlation (DIC) data.

To provide uniform axial stress distribution through the upper boundary of the model, an 8" thick I-beam was

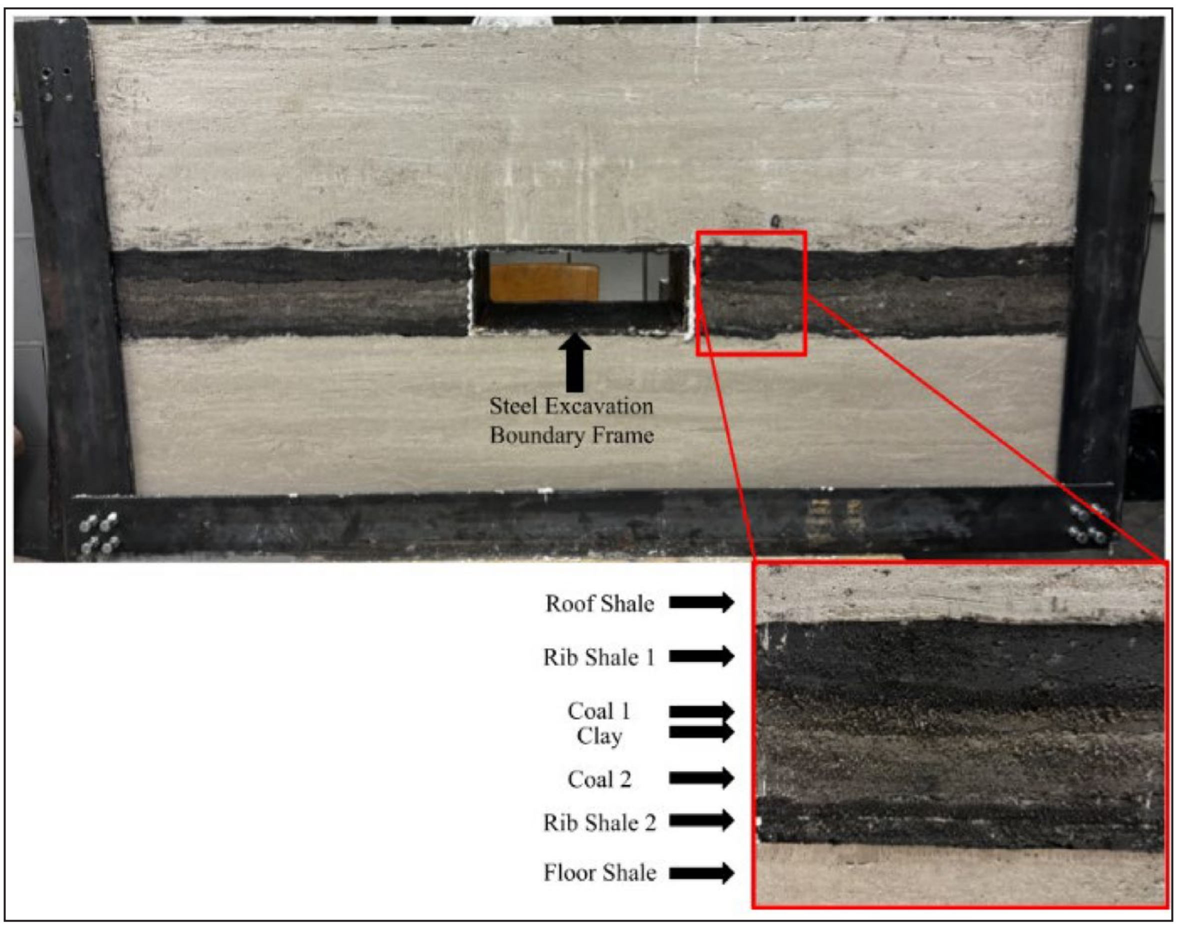

Figure 2. Constructed physical model with layers

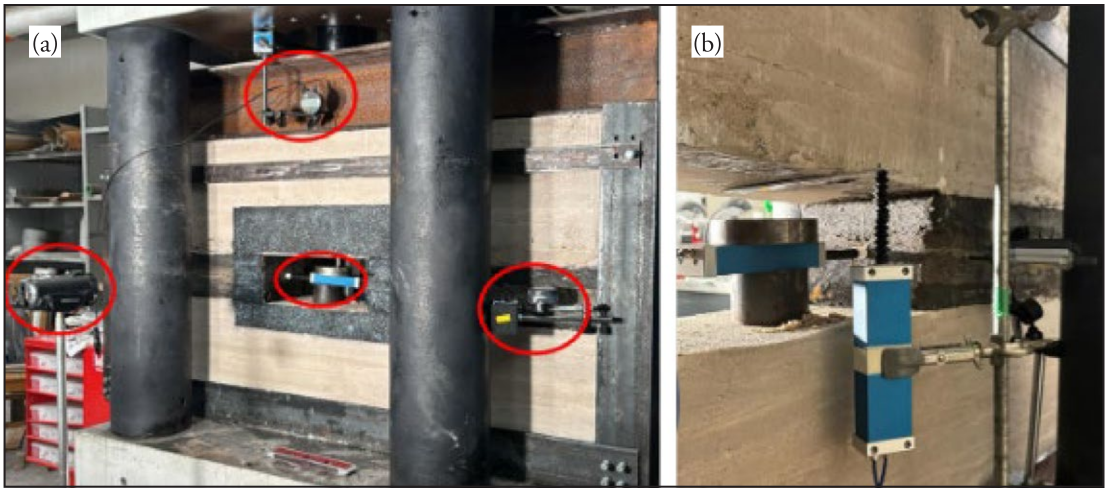

Figure 3. (a) Front and (b) back view of the model

placed between the loading frame and the model. This procedure aligns with established structural engineering research regarding wall compression tests. All the steel boundary components were coated with petroleum jelly to reduce the friction between the model and the boundaries during the experiment.

The testing protocol incorporates a multi-stage loading procedure designed to systematically apply stress increments to the model. Each stage of this procedure is monitored to ensure controlled loading and sustained loading conditions. Initially, the loading process begins with a constant displacement rate of 0.05 mm/min. This controlled rate is carefully maintained to ensure a gradual application of stress to the model. By employing a constant displacement rate, variations in loading conditions are minimized.

Once the desired stress increment of 0.1 MPa is achieved, the load is sustained for 10 minutes. This holding period is intended to allow sufficient time to observe the model behavior under the applied stress states and minimize potential shocking of the model due to rapid loading consistent with established structural testing methods. Figure 4 shows a visual representation of the applied loading procedure.

This multi-stage loading procedure, characterized by controlled displacement rates and sustained loading periods, is important for systematically increasing stress levels and capturing the model's response at each stage of the experiment.

Results of the Physical Model Tests

First Physical Model: The first experiment aimed to observe the rib response with the supported roof condition. As stated previously, the roof was supported with two I-beams. This experiment terminated when the brow failure was observed at an axial displacement of 13.59 mm. A vertical

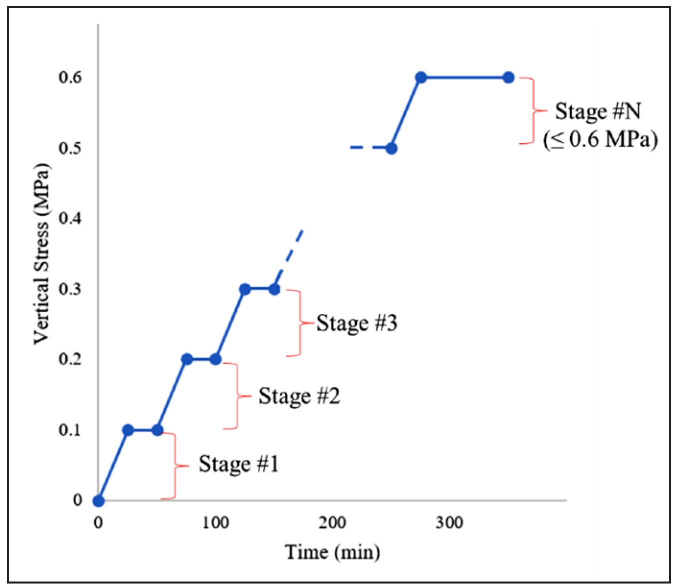

Figure 4. The loading procedure

stress-axial displacement plot was obtained by combining the data obtained from load cells and LVDTs. A simplified vertical stress-axial displacement plot is presented in Figure 5.

The coal seam kept its structural integrity throughout the end of Stage #3, corresponding to a stress level of 0.3 MPa. However, upon entering stage 4, the rib began sloughing and exceeded its elastic limit, notably observed at approximately 4 mm of rib displacement.

Consistent with the expected behavior, the weaker components of the rib (coal layers and clay) failed first during the test. The progression of failure extended to a depth

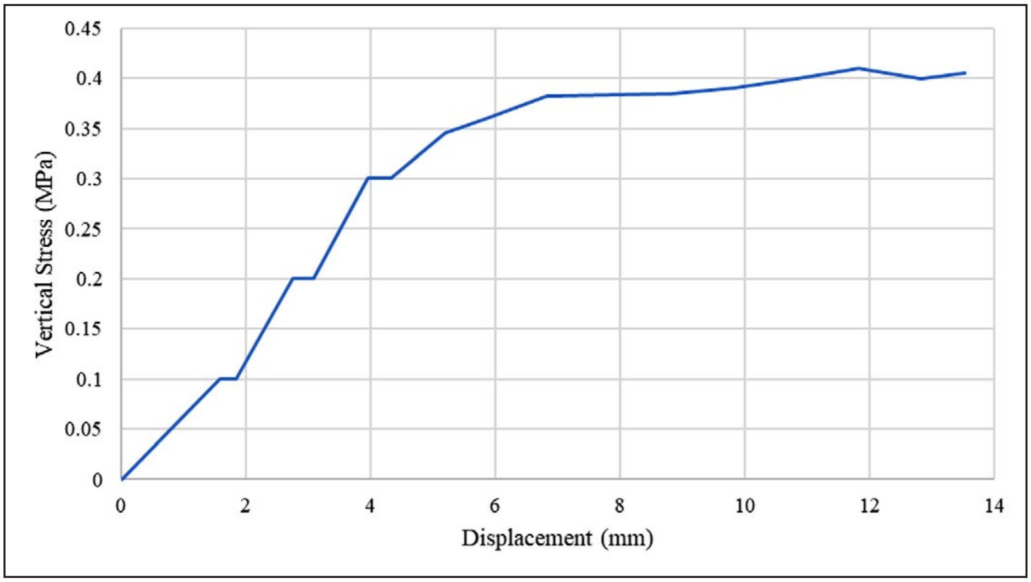

Figure 5. Stress-displacement plot (Test #1)

of approximately 5 cm (2 in) within the rib, predominantly observed on the left side of the model. Considering the geometric scaling constant (14.4) followed in the modeling methodology, this corresponds to around a 0.76 m (2.5 ft) depth of failure at the field scale. The observed brow depth of 0.76 m (2.5 ft) is highly compatible with the depth of brow values obtained in coal rib surveys. Also, in MSHA fatality reports, most measured brow depths vary between 0.6 and 0.9 meters (2 and 3 ft). It should be noted that after the model entered stage 4, although the loading continued with a constant displacement rate, it could barely reach 0.4 MPa stress levels.

Stage 4 represents a critical phase wherein the rib started to fail, subsequently leading to the formation of the brow and, finally, the brow failed. These sequential failure steps are presented in Figure 6. It is important to note that the vertical stress level (ranging from 0.35 to 0.40 MPa) did not significantly change throughout the failure steps occurring in Stage 4. As illustrated by Figure 6-a, at the end of Stage 3, the rib was mainly intact, and there were no apparent movements between the rib units. In Figure 6-b, as the major principal stress is vertical, the crushing and wedging of the rib into the excavation started at the clay parting in the mid-rib. The rib sloughing started at approximately 7.5 mm axial displacement (Figure 6-c), followed by the separation of coal layers from the surrounding shale strata (Figure 6-d). Compression-induced vertical tensile cracks in the coal layers became evident at this failure stage as well.

The relatively stronger upper shale unit in the rib triggered buckling, and the combination of the coal layer separation and the well-developed tensile cracks led to a rib failure, as presented in Figure 6-e. Vertical tension cracks were also noted at the upper rib shale at this stage. Excessive rib failure caused a fully developed brow. Subsequently, the formed brow toppled into the excavation, with dimensions 8.5 cm (3.35 in) long, 4.5 cm (1.75 in) wide, and 3.8 cm (1.5 in) thick (Figure 7). Considering the geometric scaling constant of 14.4, the failed brow dimensions are equivalent to 1.2 m (4 ft) long, 0.6 m (2 ft) wide, and 0.5 m (1.75 ft) thick in field scale.

Second Physical Model: A second test was conducted under unsupported conditions to address the observed failure in the roof unit due to the presence of support members. Although a constant displacement rate was defined in the loading stages, the control unit malfunctioned, causing total failure in the rib and invalidated the test.

Third Physical Model: Despite the second physical model test's invalidity, critical issues encountered in the previous two tests were successfully addressed. The third test was performed with unsupported conditions, a more carefully prepared speckle pattern, and 1.9 cm (0.75 in) acrylic sheets at the face and back of the model to restrict out-of-plane deformation. The roof-to-floor convergence and rib deformation response were monitored with LVDT-based transducers, as seen in Figure 8. Similarly, Figure 8 illustrates the camera location used to record the area of interest for 2D DIC analysis. Before beginning the test, all measurement instruments were zeroed to ensure that recorded values were relative to starting the test.

The experiment was terminated when the upper rib shale failure was observed at an axial displacement of 12.43 mm. A plot of load and displacement vs. time was

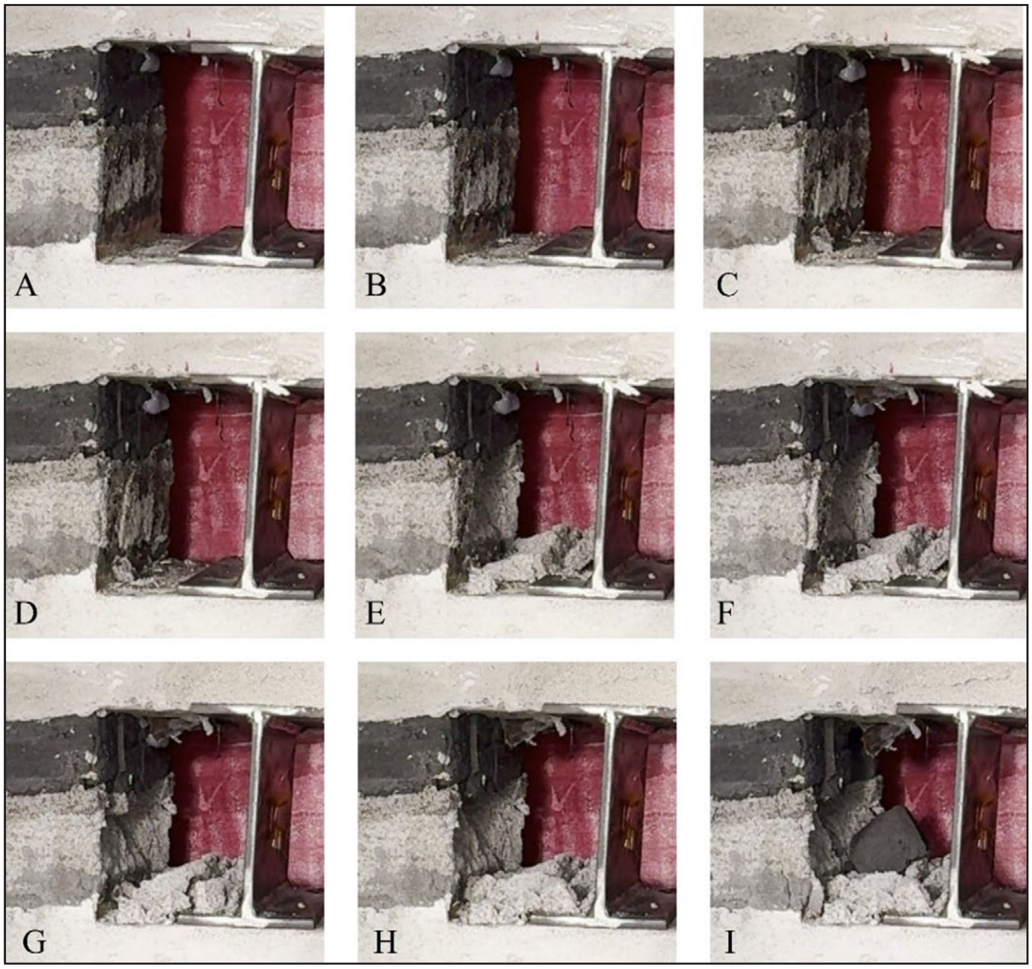

Figure 6. Sequential failure steps of the rib and the brow (Test #1)

Figure 7. Failed brow

generated from the MTS and roof-to-floor convergence, which can be seen in Figure 9.

Following the completion of the third test, brow failure was observed in the rib. Out-of-plane stress in the model caused the acrylic sheets to bind between the model and the steel frame. Despite efforts to carefully remove the acrylic sheet without disturbing the model, the failed brow crumbled inside the excavation area. Dimension measurements were instead collected by measuring the void in the upper shale unit. The brow can be seen in Figure 10.

The brow dimensions were approximately 3.2 cm (1.25 in) thick, 6.4 cm (2.5 in) long, and 3.8 cm (1.5 in) wide. When scaled up to field scale, these dimensions are 0.5 m (1.5 ft) thick, 0.9 m (3 ft) long, and 0.55 m (1.8 ft) wide. These measurements are very similar to those observed in the first test and field surveys. These similarities further highlight the relevance and applicability of these experimental findings to real-world cases. Despite the improvement in the vertical displacement DIC plots shown in Figure 11, there is still a lack of efficacy when evaluating the horizontal

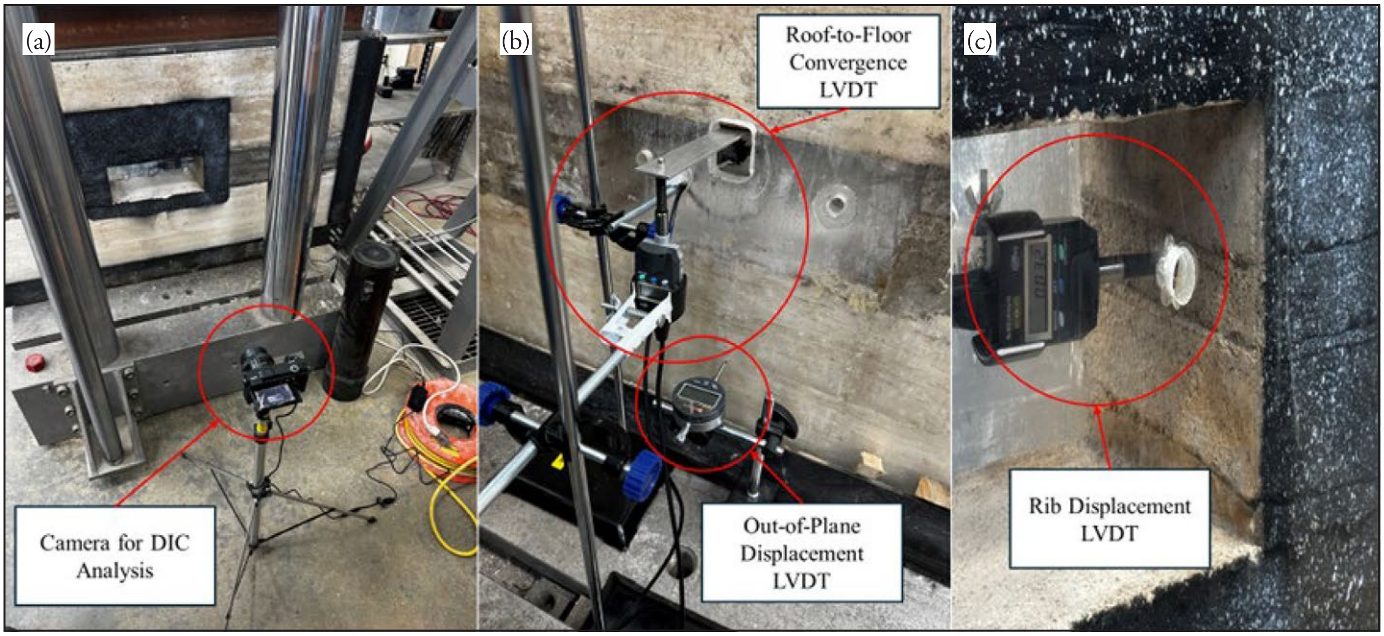

Figure 8. Experimental setup for Test 3 at the (a) front face, (b) back face, and (c) excavation zone

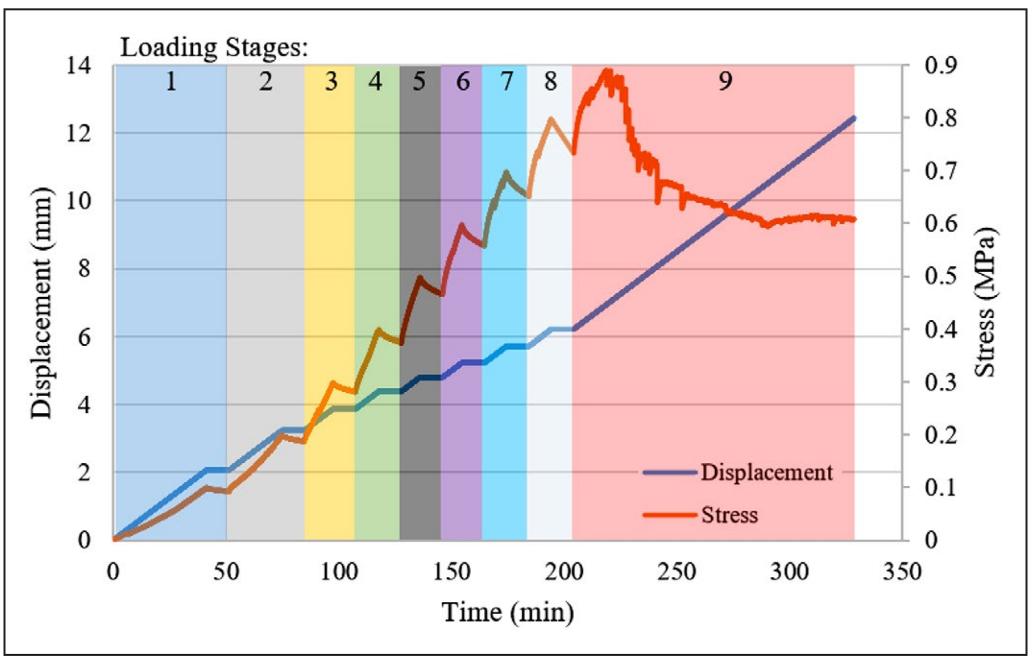

Figure 9. Stress and displacement vs. time plot of Test 3

displacement due to the horizontal movement being localized inside the excavation area rather than expressed at the faces of the model. Even though the horizontal DIC analysis was less effective, it still gives some presentation of the horizontal response in the model during loading.

PHYSICAL MODEL NUMERICAL SIMULATION

To establish an effective numerical modeling methodology for capturing the brow formation and failure mechanism, the results of the physical modeling efforts were used to

Figure 10. Failed brow observed during Test 3

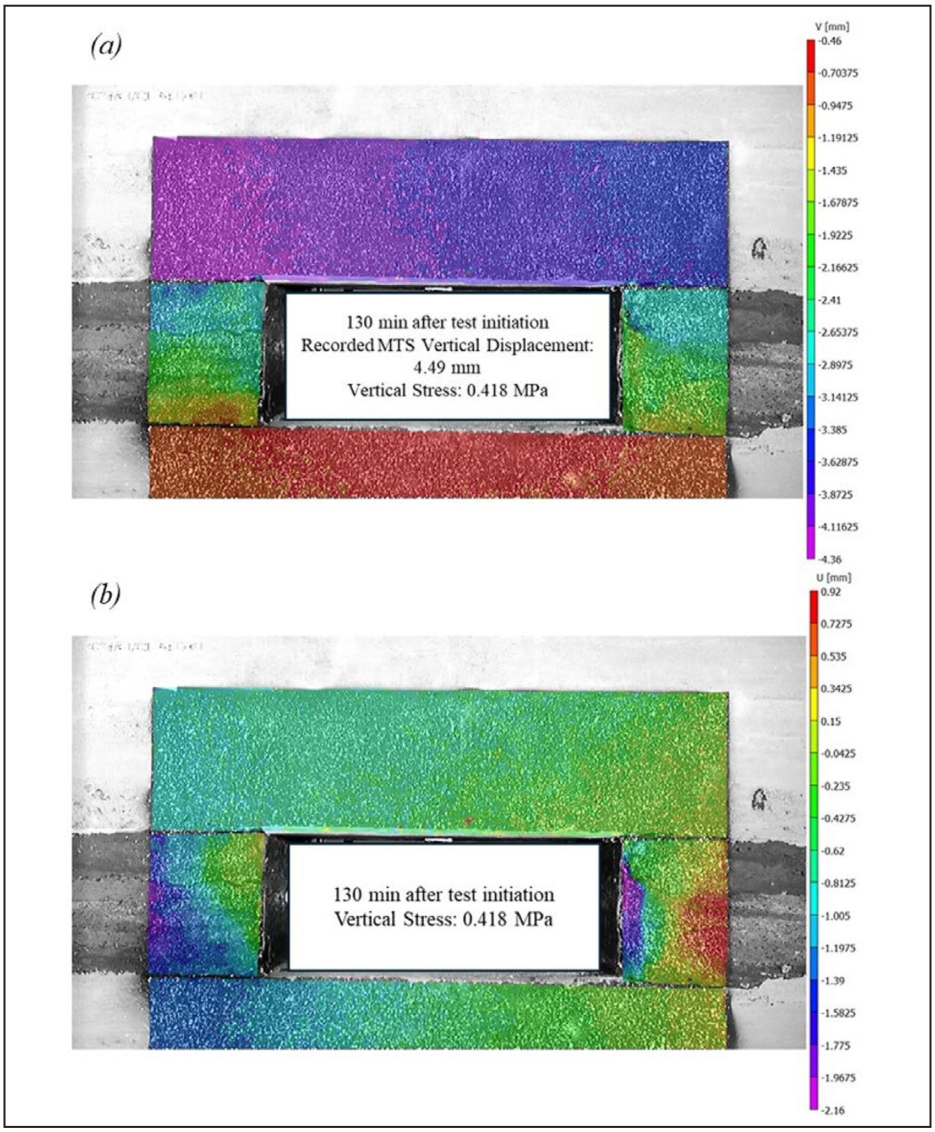

Figure 11. (a) Vertical and (b) horizontal displacement plot (Test #3)

evaluate and calibrate a coupled continuum and discontinuum bonded block modeling (BBM) approach, which explicitly captures the blocky brow failure mechanism within the area of interest while limiting computational requirements by modeling the remaining model domain as a continuum. Coupling a continuum domain with a deformable BBM approach in 3DEC allows explicit fracture modeling and the retention of an established continuum model mesh. This proved beneficial as the mesh from the physical model continuum domain could be used as the foundation for the BBM domain tetrahedral bonded block geometry. It is important to acknowledge that using tetrahedral or trigonal geometry produces inherent planes of weakness in the model mesh. While the inherent planes of weakness found in trigonal geometry are more concerning in 2D models, the continuum-BBM methodology was applied in plane strain conditions to minimize computational complexity resulting from modeling the full physical model geometry. However, research has indicated that inherent planes of weakness can be mitigated through calibration, resulting in an accurate macroscopic material response (Lemos, J. V., and Sarhosis, 2022; Lemos, J. V., 2023). This approach proved effective for capturing the blocky brow formation and failure mechanism. After determining an effective method, the physical model conditions were simulated, and the results were compared against the physical modeling test results to ensure their viability.

Modeling Targets

Within the scope of the physical modeling simulations, three main metrics were defined to compare results between the physical model tests and simulations. The first metric was the resulting brow dimensions, which were specifically targeted for replication in the physical model simulation to verify the capabilities of the coupled modeling method. The second metric evaluated was the depth of underlying rib failure captured in the numerical model before brow failure was observed. This metric ties in closely with the first, but there is also merit in observing the mode of rib failure in the simulation compared to the physical test. The final metric used was the measured axial displacement at the model's top when brow failure was observed.

Physical Model Simulation Geometry and Calibration

As mentioned previously, one of the benefits of the selected continuum-BBM approach is the retention of an already-defined model mesh. Because of this, the same model mesh and geometry were used in the model. Utilizing a coupled modeling approach required placing the fine mesh region's x-extent 6 inches from the rib face to ensure that the domain transition was not located in an area of plastic strain. The weak clay layer between the coal layers was modeled implicitly as a joint rather than explicitly as a weak layer, as the clay layer's small geometry restricted the feasibility of modeling this layer as a bonded matrix. Figure 12 illustrates the model mesh densities and layer designations. It is important to add that the fine mesh contained 4 mm edge length elements, the intermediate mesh contained 8 mm elements, and the coarse mesh contained 16 mm elements. Similarly, the discontinuum domain overlaps with the fine mesh region and transitions into the continuum domain, starting from the intermediate region outward. The material properties and constitutive models used in the continuum domain of the model were modeled with

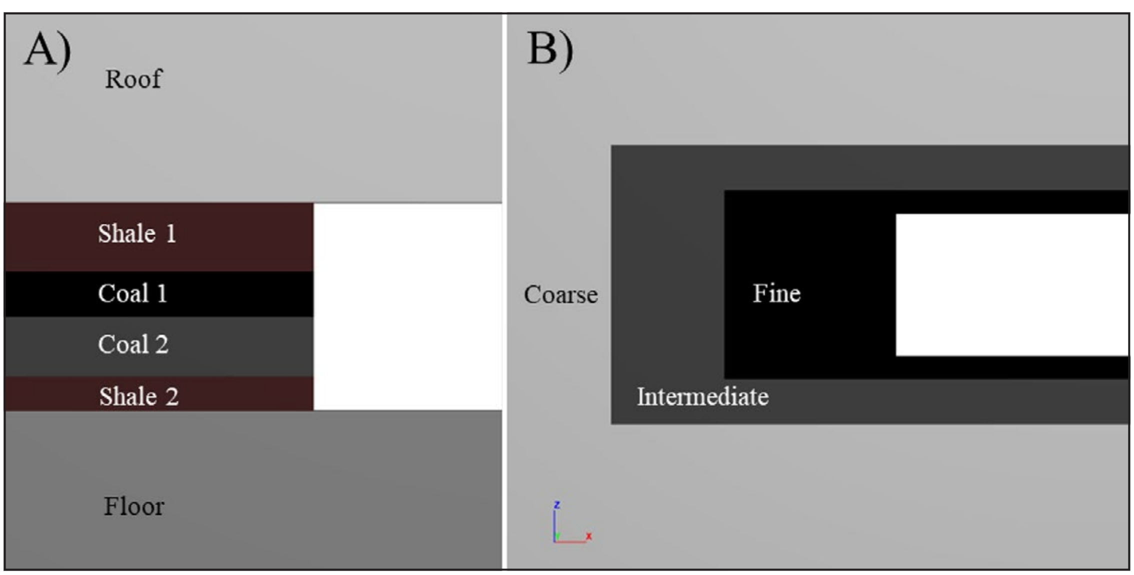

Figure 12. a) Model layer designations and b) model mesh density regions

the Coal Mass Constitutive Model developed by NIOSH researchers (Mohammed et al., 2015). This constitutive model captures the strain-softening mechanisms of coal effectively and is an effective constitutive model for simulating the engineered analogous materials used in the physical modeling tests.

The nature of the BBM approach as a discontinuous modeling method requires modeling at the micro-scale, unlike continuum modeling, which models on the macro-scale. This difference in scale requires calibration of the micro-scale material properties of the BBM matrix to ensure the bonded matrix behaves normally at the macroscopic level. This was achieved through trial-and-error calibration of the bonded matrix based on the known UCS and tensile response of the continuum equivalent to determine the required micro-scale material properties. Macro-scale material properties used in the continuum domain are provided in Table 5. The BBM properties were calibrated using 5 cm (2 in) cubes with the same fine mesh density as the full-scale model representative of the lab-scale UCS samples used during the physical modeling stage of this project. Both the uniaxial stress-strain curve and tensile response were matched for each seam layer of the simulated physical model to ensure that the BBM domain behaved like the continuum equivalent. An example of the matched stress-strain curve for the upper shale layer can be seen below in Figure 13.

It is important to recognize that this calibration approach is largely possible due to the engineered materials' lack of scale dependence as both the physical models and physical model materials' UCS samples were analyzed at the same scale, unlike the scale difference between intact rock and rock masses. Referring to Figure 13, there is excellent agreement between the elastic and peak responses of the BBM and continuum equivalent under uniaxial loading conditions. While the post-peak response does not

Table 5. Macro-scale material properties

Unit	Roof Shale	Rib Shale 1	Coal 1	Clay	Coal 2	Rib Shale 2	Floor Shale
UCS (MPa)	2.72	1	0.37	0.12	0.37	1	6.73
Young's Modulus (GPa)	0.25	0.05	0.03	0.01	0.03	0.05	1.27
Poisson's Ratio	0.25	0.25	0.25	0.25	0.25	0.25	0.25
Bulk Modulus (GPa)	0.167	0.033	0.02	0.007	0.02	0.033	0.847
Shear Modulus (GPa)	0.1	0.02	0.012	0.004	0.012	0.02	0.508

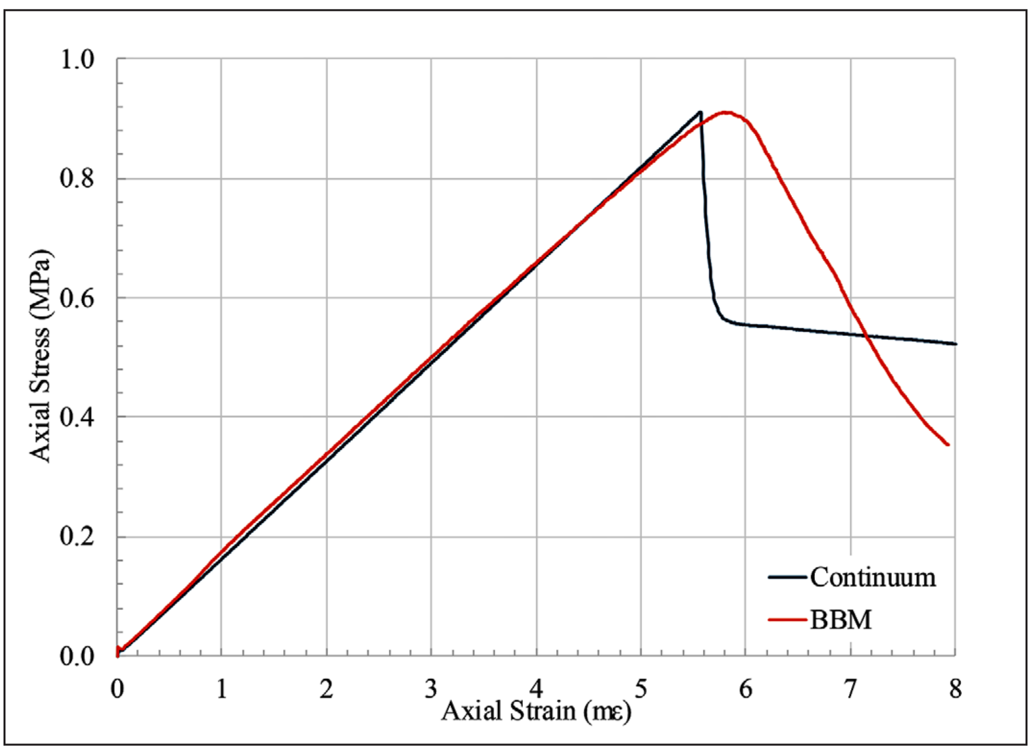

Figure 13. Shale 1 (Brow Unit) Calibration Uniaxial Stress vs. Strain Curves

Table 6. Calibrated micro-scale BBM material properties

Unit	Rib Shale 1	Coal 1	Coal 2	Rib Shale 2
Block Modulus (GPa)	1.64	2.87	1.5	0.8
Contact Normal Stiffness (GPa/m)	360	600	330	175
Contact Shear Stiffness (GPa/m)	36	60	33	17.5
Cohesion (MPa)	0.423	0.401	0.390	0.334
Tension (MPa)	0.109	0.109	0.110	0.084
Phi (Degrees)	34.6	34.6	34.6	34.6
Phi Residual (Degrees)	20	25	20	5
Dilation (Degrees)	15	15	15	5
Poisson Ratio	0.25	0.25	0.25	0.25

match as closely, this was determined to be sufficient, given 3DEC's limited contact model selection and the lack of a contact softening model. The contacts between blocks in the bonded matrix were modeled using the Mohr-Coulomb joint model, while the blocks were modeled elastically. Similarly, the joints between model units were modeled with the Mohr-Coulomb joint model as well to reduce complexity. The resulting micro-scale parameters for the bonded matrixes representing each seam layer can be seen below in Table 6, whereas the joint properties between layers are presented in Table 7.

Physical Model Simulation

A comparable loading rate was applied to the top face of the model to reflect the loading conditions of the physical model tests and avoid shocking the model. While the rib failure does not fail granularly, as would be expected, this failure mode accurately reflects the rib failure conditions observed in the third physical model test. This failure mode progresses until 7 mm of measured axial displacement, where the brow can be observed to have formed. This is illustrated in Figure 14b.

Table 7. Joint properties between model units

Joint	Brow-to-Roof	Clay	Seam
Normal Stiffness (GPa/m)	78	78	78
Shear Stiffness (GPa/m)	7.8	7.8	7.8
Cohesion (MPa)	0	0.0042	0.04
Tensile Strength (MPa)	0	0.0015	0.04
Phi (Degrees)	24	18	20
Phi Residual (Degrees)	15	15	15

The brow is considered to have failed and become mobile at approximately 8 mm of measured axial displacement, as shown in Figure 15a. This is indicated by the displacement magnitude contrast between the blocky brow and neighboring upper shale zones. Further supporting the establishment of a blocky brow failure in the model, Figure 15b provides insight into the immediate contacts in the bonded matrix around the brow, expressing failure and cohesion loss. The measured brow dimensions were 3.9 cm

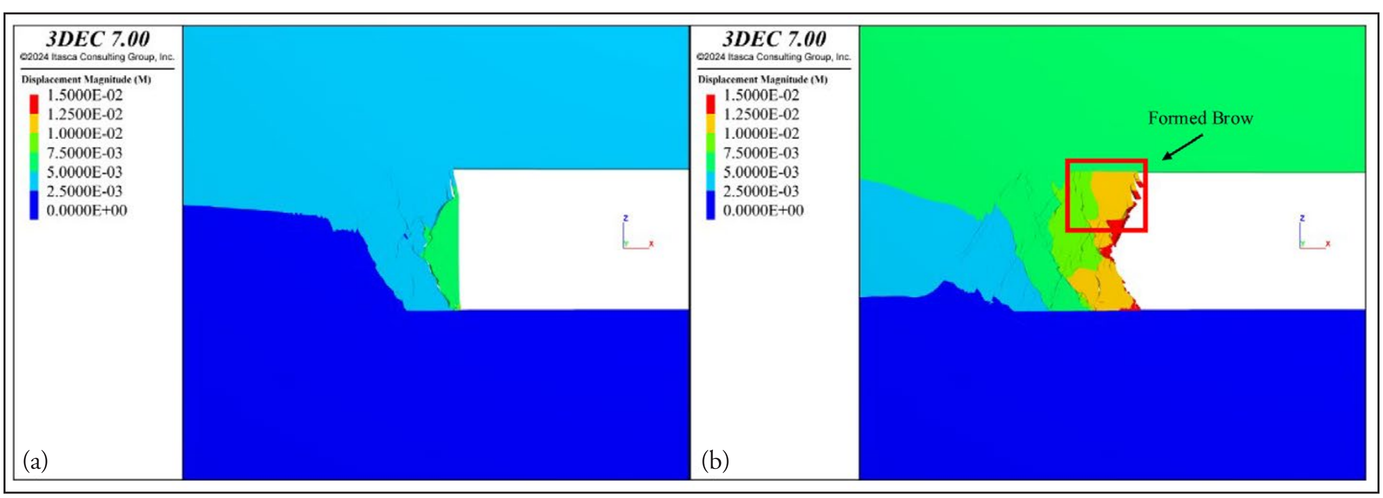

Figure 14. a) 4 mm axial displacement, b) 7 mm axial displacement

(1.55 in) deep into the rib. This matches well with the results of the third physical test as well as field observations when the dimensions are scaled by the established physical model scale factor to 0.56 m (1.9 ft).

Given the consistency of the brow dimensions compared to both the third physical model test and field observations, the established continuum-BBM modeling methodology is effective for capturing the brow's formation and failure mechanisms. It is important to recognize that the observed brow failure in the model occurred at an earlier displacement than the brow failure in the third physical model test. Despite this, there is good agreement between the numerical model and physical model brow dimensions and depth of rib failure. Similarly, the rib failure mechanism in the numerical model simulation closely resembles what was observed during the third physical model test. This closeness to observed and measured metrics in the field surveys and physical modeling tests lends itself to the applicability of this modeling methodology to capture complex coal hazards such as coal or rock brow failures.

CONCLUSIONS

The outcomes of this study further support the use of physical modeling methods as a means of collecting data that are otherwise impossible or extremely difficult to achieve in complex field conditions such as brow formation and failure. Despite this, it is important to acknowledge the limitations of the physical model testing results. While the first test observed a brow formation and failure, the presence of support members caused compressional failure in the roof unit of the physical model. Because of the roof unit's failure, accurate stress transfer into the upper shale unit could not be guaranteed. Another problem occurred due to the choice of pouring material into the model frame for in-place curing. Despite extreme care being taken to ensure flatness between layer pours, slight undulation was still observed at some points in the models. Considering these limitations, however, the resulting brow dimensions from the first and third tests are very close to each other and match well with the selected case study's measured brow dimensions, as illustrated in Table 8.

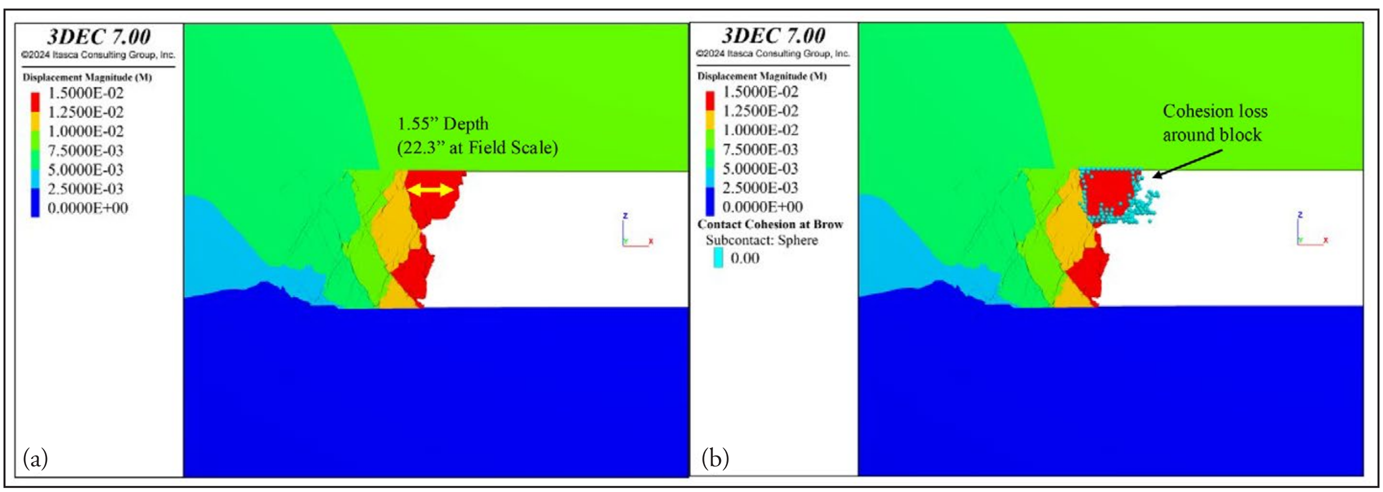

Figure 15. a) Failed brow depth into rib, b) cohesion loss around brow

Table 8. Key metrics from physical model experiments

	Test Number		
Test Condition	**1**	**2**	**3**
Maximum Applied Displacement (mm)	13.59	14.89	12.43
Maximum Vertical Stress (MPa)	0.4	0.36	0.89
Face/Back Boundary Conditions	Free	Free	Restricted
Test Duration (Minutes)	270	150	330
Excavation Supported	Yes	No	No
Brow Observed	Yes	No	Yes
Brow Dimensions (cm)	4.5 × 8.5 × 3.8	-	3.2 × 6.4 × 3.8

These results support that physical modeling is a powerful tool for case-specific analysis in controlled laboratory environments. A summary of key takeaways is offered below:

- Two of the three physical model experiments resulted in similar brow dimensions. The first test resulted in a brow with dimensions 4.5 cm wide, 8.5 cm long, and 3.8 cm thick; the third test's brow was 3.2 cm wide, 6.4 cm long, and 3.8 cm thick. Despite the invalidity of test 1, the brow dimensions are consistent with each other and the field observations.
- Like the closeness of the brow dimensions, the depth of failure observed in the models' rib was consistent with each other. The first test observed a depth of failure of 4.5 cm, while the third test observed a depth of failure of 3.2 cm. The depth of failure observations also match well with those collected in the field. This illustrates the usefulness of the collected data.
- The driving mechanisms behind brow formation and failure were better understood due to the physical model providing a controlled environment for failure progression. As seen by the sloughing response, the clay parting and coal layers in the rib failed predominantly in shear. The upper shale layer, where the brow formed, was clearly seen to fail in tension based on the presence and progression of tension cracks at the rib face and the blocky condition of the brow post-failure. Similarly, a clear separation from the rib could be seen behind the brow following the test conclusion.
- The determination of analogous material mixtures is a time- and resource-dependent process. It is important to highlight that there is no systematic process to achieve the required analogous material properties. Thus, a process was designed to create and test multiple mixture ratios and determine the mixtures exhibiting properties closest to the selected critical case.
- Much like the determination of analogous mixtures, the design and creation of the physical model is entirely dependent on the case and available resources; there is no proven methodology that fits all. As such, a model to best represent the selected critical case was created while facilitating the collection of key data at a laboratory scale.

The results from the physical model tests provided useful data for evaluating a coupled continuum and BBM methodology. The results of this approach illustrated good agreement with the depth of failure in the rib and the resulting brow dimensions after brow failure occurred in the upper shale unit. It is important to acknowledge that failure was observed in the numerical model at a lower applied displacement level than what was observed in the physical model tests. This difference is largely attributed to limitations in the available contact models to define the bond behavior in 3DEC and reflect a more accurate post-peak macroscopic softening response as is observed in coal. Considering this, the results of the numerical modeling methodology present an effective means of capturing explicit failure and separation of the brow after formation as a result of continued loading conditions and underlying coal sloughing. The implications of this are that physical modeling results can be used to validate a numerical model representing complex brow conditions, which can be further explored numerically for an enhanced understanding of key mechanisms governing brow stability in myriad coal mine environments.

ACKNOWLEDGMENTS

This work was financially supported by The National Institute of Occupational Safety and Health (NIOSH) under the contract No. 75D30122C14756.

REFERENCES

Esterhuizen, G. S., Bajpayee, T. S., Ellenberger, J. L., & Murphy, M. M. (2013a). Practical estimation of rock properties for modeling bedded coal mine strata using the Coal Mine Roof Rating. In ARMA US Rock Mechanics/Geomechanics Symposium (pp. ARMA-2013). ARMA.

Fang, F., Shu, C., & Wang, H. (2020). Physical simulation of upper protective coal layer mining with different coal seam inclinations. Energy Science & Engineering, 8(9), 3103–3116.

Huang, Q., & Cao, J. (2019). Research on coal pillar malposition distance based on coupling control of three-field in shallow buried closely spaced multi-seam mining, China. Energies, 12(3), 462.

Jones, T., Mohamed, K., & Klemetti, T. (2014). Investigating the contributing factors to rib fatalities through historical analysis. In Proceedings of the 33rd International Conference on Ground Control in Mining (pp. 113–22).

Kang, H., Lou, J., Gao, F., Yang, J., & Li, J. (2018). A physical and numerical investigation of sudden massive roof collapse during longwall coal retreat mining. International Journal of Coal Geology, 188, 25–36.

Kong, D., Pu, S., Cheng, Z., Wu, G., & Liu, Y. (2021). Coordinated deformation mechanism of the to coal and filling body of gob-side entry retaining in a fully mechanized caving face. International Journal of Geomechanics, 21(4), 04021030.

Li, A., Ji, B., Ma, Q., Ji, Y., Mu, Q., Zhang, W., ... & Zhao, C. (2022). Physical simulation study on grouting water plugging of flexible isolation layer in coal seam mining. Scientific Reports, 12(1), 875.

Lemos, J. V. (2023). Application of Bonded-Block Models to Rock Failure Analysis. *Applied Sciences*, *13*(22), 12207–12207. DOI: 10.3390/app132212207.

Lemos, J. V., & Sarhosis, V. (2022). Discrete Element Bonded-Block Models for Detailed Analysis of Masonry. *Infrastructures*, *7*(3), 31. DOI: 10.3390/infrastructures7030031.

Mohamed, K. M., Tulu, I. B., and T. Klemetti. "Numerical Simulation of Deformation and Failure Process of Coal-Mass." Paper presented at the 49th U.S. Rock Mechanics/Geomechanics Symposium, San Francisco, California, June 2015.

MSHA. (2025). Fatality Reports. https://www.msha.gov/data-and-reports/fatality-reports/search.

Obert, L. & Duvall, W.I. (1967): Rock mechanics and the design of structures in rock, John Wiley & Sons, 650 p.

Singh, T. N., & Farmer, I. W. (1985). A physical model of an underground coal mine prototype. International Journal of Mining Engineering, 3, 319–326.

Yang, J. H., Yu, X., Yang, Y., & Yang, Z. Q. (2018). Physical simulation and theoretical evolution for ground fissures triggered by underground coal mining. PLoS One, 13(3), e0192886.

Zhai, X., Wu, J., Dou, Z., Huang, K., Wang, G., & Ma, Y. (2017). Water Inrush Mechanism Caused by Fault Activation Based on Stress Evolution of Surrounding Rock of Key Aquifer. Journal of Engineering Science & Technology Review, 10(6).

Society for Mining, Metallurgy & Exploration

MINEXCHANGE

2026 SME ANNUAL CONFERENCE & EXPO

FEBRUARY 22-25, 2026

SALT LAKE CITY, UTAH

2026 Preprints

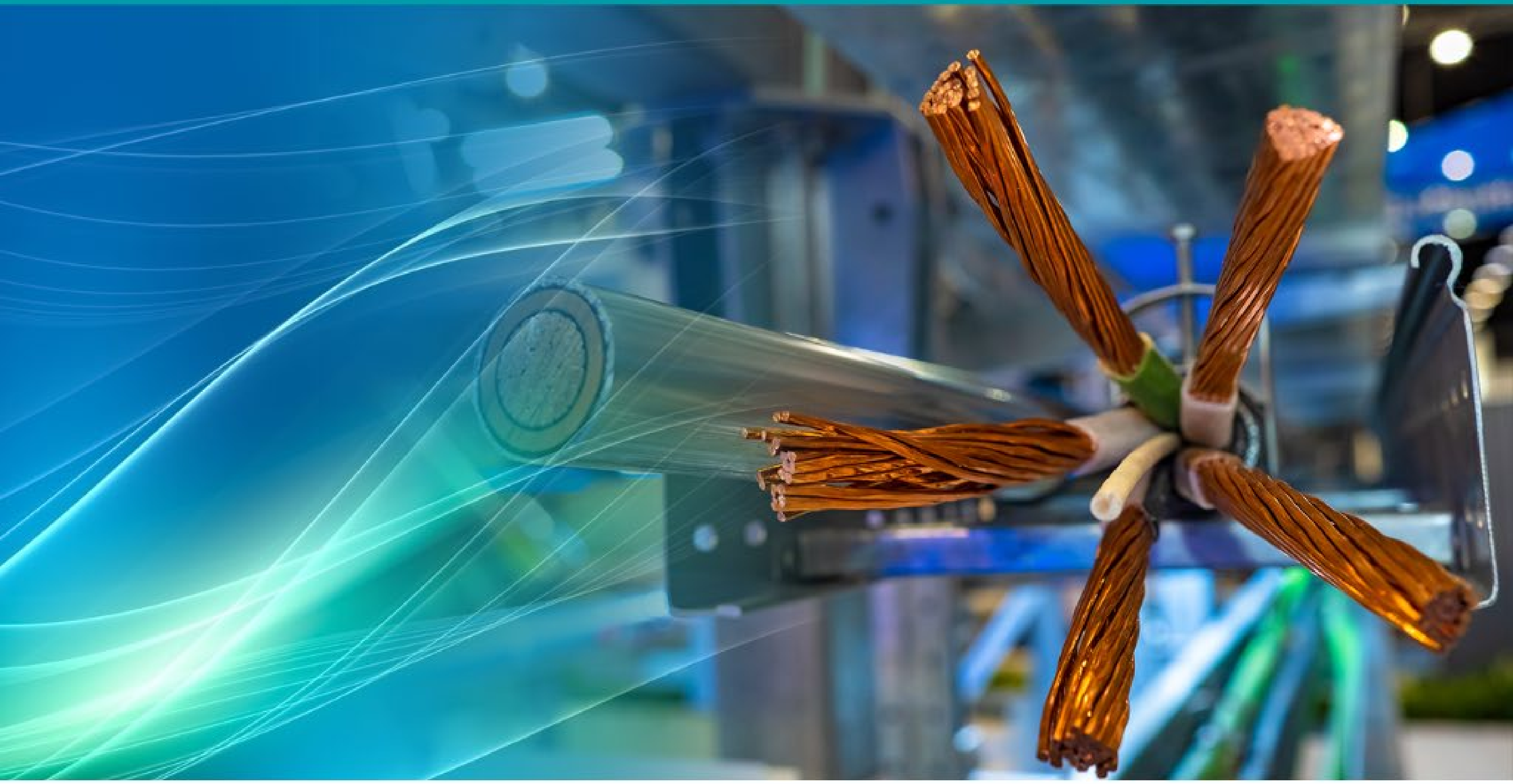

Society for Mining, Metallurgy & Exploration (SME)
12999 E. Adam Aircraft Circle
Englewood, Colorado, USA 80112
(303) 948-4200 / (800) 763-3132
www.smenet.org

SME advances the worldwide mining and underground construction community through information exchange and professional development.